



One-pot microwave mediated growth of heterostructured ZnO@AlSi as a potential dual-function eco-catalyst for treating hazardous pollutants in water resources

P.S. Suchithra*, C.P. Shadiya, A. Peer Mohamed, P. Velusamy, S. Ananthakumar*

Functional Materials Section, Materials Science and Technology Division, National Institute for Interdisciplinary Science and Technology (CSIR), Trivandrum 695019, Kerala, India

ARTICLE INFO

Article history:

Received 16 July 2012

Received in revised form 10 October 2012

Accepted 14 October 2012

Available online 23 October 2012

Keywords:

ZnO

Aluminosilicates

Cr(VI) photoreduction

Phenol photooxidation

Methylene blue

ABSTRACT

Dual function, eco-catalyst material had been designed with nano ZnO@aluminosilicate mineral (ZnO@AlSi) and processed via microwave assisted in situ intercalation and crystal growth reactions. Dual function of ZnO@AlSi was confirmed by the simultaneous adsorption and UV photoreduction of carcinogenic Cr(VI) to non-toxic Cr(III) and photooxidation of phenol and methylene blue dye (MB); a co-existed model system was simulated and prepared together in laboratory conditions. Single phase nano ZnO and ion exchanged AlSi layered silicates were also separately prepared for comparisons with ZnO@AlSi system. All these materials were characterized for BET, DLS, TGA, SEM, TEM, UV–visible and fluorescence spectrophotometry to analyze structural, thermal, morphological, and optical properties. It was seen that the inherent silicate layered structure significantly restricted the growth of ZnO, resulting in mesoporous, UV-active ZnO@AlSi heterogeneous nanocatalyst. An effective adsorption of Cr(VI), phenol and MB to the extent of 99% and the transformation of Cr(VI) to Cr(III) through photoreduction, and decomposition of phenol and MB by photooxidation followed by mineralization were achieved at once. This synergic adsorption and photodecomposition effects could not be found together in single phase nano ZnO as well as ion exchanged AlSi system. The kinetic photo-experiments indicated that reduction of Cr(VI) and degradation of phenol and MB by ZnO@AlSi followed Langmuir–Hinshelwood first-order kinetic model. The investigation of ZnO@AlSi at Cr(VI)/phenol and Cr(VI)/MB binary systems displayed high decontamination performance of ZnO@AlSi than in single pollutant system due to the arresting of electron–hole pair recombination via consuming both the members in separate redox half-reactions. Alternatively, life time of catalyst was found decreased in organic–inorganic pollutant system compared to single component systems. In summary, a dual function catalyst was designed through a facile technique and validated for the cost-effective removal and decomposition of organic and inorganic pollutants simultaneously in the complex wastewater.

© 2012 Elsevier B.V. All rights reserved.

1. Introduction

Chromium is a toxic, mobile heavy metal often discharged together with hazardous organics such as dyes and phenols from industrial fields that engaged in electroplating, leather tanning, metal finishing, textile dyeing, and chromate chemical manufacturing [1,2]. Chromium usually exists as Cr(III) and Cr(VI) species in the environment and Cr(VI) is reported to be 100 times more toxic than Cr(III). US-EPA has set the maximum contamination level of Cr(VI) in aquatic medium to be 0.05 mg/L, while WHO recommends still a lower toxic limit of 0.005 mg/L [3,4]. Phenols generally constitute 11th of the 126 chemicals, which have been designated as

priority-pollutants by the US environment protection agency. Similarly acute exposure to methylene blue dye (MB) can seriously harm human health, particularly as breathing troubles and skin problems [5]. Therefore removal of these toxic pollutants from industry discharge is a matter of great concern to save the aquatic environment. Mostly these toxic species are very stable to sunlight and natural oxidizing agents and resist biodegradation. Till date, techniques like biological treatments, reverse osmosis, chemical precipitation and adsorption methods are widely employed for the separation and purification of these contaminants. However, industries are striving to minimize the waste-treatment costs as much as possible. Hence the development of industrially viable, cost-effective, eco-friendly adsorbents with attractive multiple functions such as adsorption, conversion and decomposition is being considered seriously by environmental scientists and researchers. Layered silicates, a naturally occurred mesoporous nanomaterials, have been one of most preferred industrial adsorbent due to effective adsorption of toxic

* Corresponding authors. Tel.: +91 4712515289.

E-mail addresses: schithraps@gmail.com (P.S. Suchithra), ananthakumar70@gmail.com (S. Ananthakumar).

pollutants, easy availability, eco friendly nature and low price [6–8]. Unfortunately, adsorption alone does not provide any permanent solution because the toxic elements are actually transformed from one phase to another phase and remain as such producing toxic sludge which further require disposal to landfill with serious environmental health implications. In addition to the physico-chemical trapping, conversion to non-toxic form or decomposition of these pollutants would be more ideal. Silicate adsorbents engineered with photocatalytic ingredients; for example, tailoring the aluminosilicate inter-layers and its surfaces with nanostructured TiO_2 , ZnO , CeO_2 , and SnO_2 semiconducting photocatalysts (popular in breaking the contaminant organic molecules to non toxic atmospheric gases like CO_2 and H_2O) can make them multifunctional composites and heterogeneous catalysts by hybridizing adsorption and photocatalytic efficiencies of both members [9]. Among industrial photocatalysts, nano scale ZnO and TiO_2 are the most preferred ones that show multiple functions like hydrophobicity, wide selectivity to ions and gases, fast photo-degradation, photo-reduction and bio active conversions. ZnO has better advantage in a way that it can absorb over a larger fraction of UV spectrum and its nanostructures can be attained at low temperature [10]. However, ZnO is not stable in acidic conditions and also show rapid deactivation in bulk due to increased tendency of aggregation [11]. Therefore, factors such as inhibition of spontaneous growth at elevated temperatures, prevention of aggregation, surface protection against alkali and acid attack needed to be controlled by suitable manner. An approach frequently used is the immobilization of ZnO catalyst on porous inorganic matrices such as activated carbon, MCM-41, SBA silica, zeolites and layered silicates [10–12]. The recently increasing interest of the research community in the ZnO /clay system reveals the potential of this heterostructured hybrids for various applications [13,14]. However exploration of this system for environmental pollutant degradation is still limited. Immobilized ZnO in cetyl trimethyl ammonium chloride modified clay is recently reported to decompose MB in presence of a strong chemical oxidant (H_2O_2) and another group reported about its efficiency for photodecomposition of phenol [15,16]. These studies dragged our attention to the possible use of photoactive nano ZnO in natural adsorbent like aluminosilicates for the decontamination of multicomponent complex pollutant systems containing both toxic metal ions and hazardous organics that are more similar to the real environment [17–19].

Hence in this work ZnO encapsulated aluminosilicate (designated here after as ZnO@AlSi) was designed through microwave assisted in situ nucleation and growth which is not tried by any other researchers so far to the best of our knowledge. Growth features of nano ZnO in AlSi matrix under microwave irradiation, agglomeration tendency of ZnO nanoparticles, photo oxidation and photo reduction synergic effect without using any environmentally incompatible strong oxidants are studied and reported. Also degradation of catalyst is analyzed via conducting adsorption/photocatalysis experiments consecutively for three cycles with three single-component systems (Cr(VI) , MB and phenol) and two bi-component systems (Cr(VI) /MB and Cr(VI) /phenol). The results presented in this work describe the behaviour of ZnO@AlSi as not only an adsorbent but also as a catalyst for treating the complex multiple pollutants in aquatic environment.

2. Experimental

2.1. Materials

Zinc nitrate hexahydrate ($\text{Zn(NO}_3)_2 \cdot 6\text{H}_2\text{O}$, 99.0% purity), ammonium hydroxide (NH_4OH), methylene blue, phenol, potassium dichromate ($\text{K}_2\text{Cr}_2\text{O}_7$, 99.9% purity) were purchased from SD

Fine-Chem Ltd, Mumbai. Indian origin aluminosilicate clay mineral (Bentonite) and 1,5-diphenyl carbazide [$(\text{C}_6\text{H}_5\text{NHNH})_2\text{CO}$] were purchased from Central Drug House Pvt Ltd, Mumbai. Sulphuric acid (H_2SO_4 , 99.0% purity) and polyethylene glycol (PEG 4000) were obtained from E-Merck, India Ltd. All chemicals were of analytical grade and were used without further purification. All solutions were prepared with deionised water of specific conductivity less than $1 \mu\text{ohm/cm}$.

2.2. Modification of aluminosilicate clay mineral

Raw clay contains impurities and agglomerated clusters. Therefore it was purified first using the following procedure: 5 g raw clay was dissolved in 1000 ml distilled water with vigorous stirring for 24 h. The clay suspension was then separated from sedimented impurities and centrifuged using REMI R25 at 7000 rpm. The settled particles were resuspended in 1000 mL deionised water and stirred again for 24 h, and repeatedly centrifuged several times to obtain submicrometer size clay particles. The purified clay was then subjected to ion exchange with Na^+ . The Na-saturated clay was prepared using established procedures [20]: Briefly, 10 g of the purified clay was stirred with 1 L of 1.0 M NaCl solution for 12 h. The solid mass was then centrifuged and washed repeatedly with distilled water until the clay is Cl^- free. Confirmation test was conducted with 10% silver nitrate solution. The ion exchanged clay was finally dried at 80°C .

2.2.1. Preparation of nano clay (AlSi)

In order to get nano range particles and to achieve optimum swelling, 10 grams of ion exchanged clay in 250 ml distilled water were stirred continuously using a magnetic stirrer for 30 min to obtain a homogenous dispersion and further sonicated for 30 min and was kept undisturbed for 4 h. It is then centrifuged to separate the yellow coloured suspension which is then dried at 80°C to get clay particles fraction with a size range of 100–200 nm, as evidenced by photon correlation spectroscopy.

2.3. Microwave assisted synthesis of ZnO

2 g of $\text{Zn(NO}_3)_2 \cdot 6\text{H}_2\text{O}$ and 0.6 g of PEG were dissolved in 500 mL distilled water and stirred for 30 min. To this NH_4OH solution were added drop wise with vigorous stirring till the solution pH reached 8.5. The resultant white precipitate was then subjected to microwave irradiation [450 W, 2.45 GHz] for 4 min and then cooled to room temperature. After microwave treatment, the white precipitate was collected, washed and centrifuged several times with hot water and finally with ethanol. The nano ZnO was then dried at 70°C and ground and kept in desiccators for further use.

2.4. Microwave assisted synthesis of ZnO@AlSi

ZnO@AlSi was prepared as described below. To the transparent zinc nitrate hexahydrate and PEG solution, 100 mL of already sonicated and swelled AlSi (0.5 g) was added drop wise with vigorous stirring. The reactants mixture was stirred for 30 min and again homogenized through sonication for 30 min. To this NH_4OH solution was added till the solution pH reached 8.5. The resulted precipitate was then microwave irradiated for 4 min. Finally the reaction was stopped and naturally cooled. The resultant precipitate was collected and centrifuged with hot water several times and at the end with ethanol. The washed precipitate was dried at 70°C . The product was designated as ZnO@AlSi which was then ground, sieved and kept in desiccators for further use.

2.5. Adsorption and photo activity studies

Blank experiments were carried out initially using AlSi, ZnO and ZnO@AlSi, under dark and UV and visible light to analyze adsorption and photocatalytic efficiency, respectively. 0.1 g each of AlSi, ZnO and ZnO@AlSi and 50 ml of water polluted with MB (50 mg/L) was stirred in dark to determine the extent of adsorption of MB to the catalyst surface. A 2 ml of sample was withdrawn in fixed time interval (5 min to 2 h at the maximum) for UV–visible spectroscopic analysis. After adsorption was reached equilibrium, the reaction vessel was transferred to photoreactor (Rayonet, Netherlands) containing 15 W tubes (Philips G15 T8) as the UV-source, which emitted the UV radiation with the wavelength within the range of 200–400 nm (corresponding to the photon energy range of 3.07–6.14 eV) and stirred for another 4–5 h. The visible illumination was provided by a high pressure mercury lamp, which emits light in the wavelength range of 410–800 nm with an intensity of 7 mW/cm². Three UV filters were used to eliminate UV radiation, if any, in the emitted light. A 2 ml of sample was withdrawn in fixed time interval and centrifuged prior to for UV–visible spectroscopic analysis. All other adsorption/photocatalytic experiments reported in this study were done only with ZnO@AlSi but the pollutant system ranged from single systems (MB and Cr(VI) of varying concentration from 10 to 100 mg/L) to binary systems (Cr(VI)/MB and Cr(VI)/phenol).

The concentration of pollutants was monitored from the absorbance peak intensity before and after the adsorption and photocatalysis. The characteristic absorption band of methylene blue and phenol occurred at 656 and 270 nm, respectively. Cr(VI) concentration was estimated spectrophotometrically using the conventional colorimetric method by measuring the purple complex of Cr(VI) with 1,5-diphenylcarbazide in acidic medium at 540 nm against a reagent blank in UV–visible spectrophotometer. The total chromium which is the sum of tri- and hexavalent (Cr(T) = Cr(VI) + Cr(III)) was measured to establish the effectiveness of photocatalytic reduction process by AAS in combination with air–acetylene flame at 429 nm wavelength and slit width of 0.5 nm.

3. Results and discussion

3.1. Synthesis, morphology and physical characterizations

Nanostructured ZnO growth into various morphologies is reported to be a net effect of self-organization and, hierarchical assembly of the zinc nuclei due to its differential polar surfaces at the given reaction conditions. The dimensional control and specific morphology is achieved through structure directing agents. In the same way, the rigid silicate matrix controls the growth patterns when the Zn-nuclei are embedded within the silicate layers. Silicate layers are laminated structures and in this work the immobilization of Zn-ions was accomplished by complexing with PEG. It is infact a most preferred capping molecule for nano-ZnO. PEG is a hydrogel that binds effectively with the silicates and ideally promote the intercalation of Zn-ions through hydrogen bonding. PEG intercalation in bentonite clay is well documented and widely reported [21,22]. PEG modified silicate layers readily absorb microwaves due to highly polar surface hydroxyls of clays as well as PEG molecules. The rapid dipole movements generate thermal gradients which act as driving force for the crystal growth. During the microwave treatment the pre hydrolysed zinc nuclei self-assemble in the interlayers of AlSi substrates and the microwave irradiation cause multiple reverse dipoles that result in micro-thermal dielectric heating. This transforms the partially hydrolyzed nuclei to well crystalline ZnO. The in situ homogeneous dispersion of complex zinc oxy hydroxide moieties in the interlayered AlSi structure generates uniform

distribution of the nanostructures. In this work we have seen the formation of crystalline ZnO grow into well-oriented flower like architecture. The microwaves also facilitate cross linking of sub-nano size ZnO particles with silanol functional groups lead to hybrid nano structures. The Al–Si–Zn bonding is possibly occurred through hydrogen bonding. The morphology and crystal growth control by Al–Si matrix is clearly seen in the particle size and TEM analysis. The particle size distribution of the AlSi, single-phase ZnO and intercalated ZnO@AlSi as studied by photon correlation spectra (PCS) on dynamic light scattering (DLS) technique is shown in supplementary information (Fig. S1). The particle size curves displayed bi-modal distribution curve for AlSi and a broad uni-modal particle size distribution for ZnO. The sample ZnO@AlSi showed impressively a narrow size distribution curve with an average particle size of 110 nm. This value is nearly 10 times lesser compared to single-phase ZnO. In case of free growth, the single phase ZnO has grown in uncontrolled manner containing multi-branched nano thick ZnO sheets assembled in flower fashion. The growth of ZnO sheets shows uni-modal distribution with a full width at half maximum (FWHM) value of 1385.7 nm. This is a strong evidence for grain growth inhibition by silicate structures. The nano clay, AlSi, displayed maximum number of particles with narrow size distribution around 207 nm with associated less intense secondary size distribution in a much wider range of particles in the size region of 800–1300 nm with the FWHM of 1054.4 nm. The larger particle size is an indication for agglomeration of small ZnO crystallites.

The TEM image (Fig. 1) of AlSi showed structurally deformed randomly aligned exfoliated fibrous bundle structures due to repeated sonication and mechanical stirring. The SAED pattern of AlSi confirmed the crystalline nature. The freely grown ZnO displayed distinct multilayered flower assembly grown from a centralized primary parent nuclei with diameter ranged from 2.1 to 2.3 μm comprising of tightly packed petals with linear dimension of 0.6 μm . Generally flower like ZnO is obtained from hydrothermal synthesis. It is reported that the anisotropic growth and hence morphology of ZnO is greatly influenced by pH value because of its effect on the initial nuclei and growth environment of ZnO [23,24]. In case of in situ intercalated hybrids the ZnO morphology is completely changed. As shown, ZnO@AlSi displayed hexagonal platelet shaped ZnO crystallites of varying sizes ranging from 3.6 to 146.7 nm. The surface of the platelets shows high roughness indicating the restricted growth feature of ZnO crystallites. The X-ray diffraction of AlSi and ZnO flowers clearly indicate their multicrystalline nature. However ZnO@AlSi system showed high level of crystallinity compared to ZnO.

The results on the bulk crystalline structure of AlSi, ZnO and ZnO@AlSi as observed from the powder X-ray diffraction analyses were presented in Fig. 2(a). As shown, XRD pattern of AlSi (Na⁺ exchanged) was typical of very crystalline clay. The high intensity peak (001) at $2\theta = 5.07^\circ$ with basal spacing of 17.41 Å indicates the interlayer distance in the AlSi structure, which upon hybridization with ZnO shifted to $2\theta = 3.21$ and 1.97° with basal spacing of 27.48 and 44.89 Å, respectively, strongly evidencing the intercalated heterostructure of ZnO@AlSi [14]. The peak of 4.43 Å at (002) plane further implied 2:1 mineral type. The diffraction peaks with basal spacing of 2.81, 2.60, 2.48, 1.91, 1.63 and 1.48 in the spectrum of ZnO could be indexed to (100), (002), (101), (102), (110) and (103) crystal planes of zincite phase of ZnO (JCPDS 76-0704). The characteristic peaks of ZnO and AlSi were retained in the ZnO@AlSi indicating that the hybridization with AlSi did not influence the crystalline structure of both components. The decreased peak intensity in ZnO@AlSi could be attributed to high dispersion of ZnO particles in the internal structure of AlSi. Considering the results obtained from XRD, TEM and PCS, it was concluded that the ZnO species were grown in the interlayer space and in the mesopores formed by the house-of-cards stacking of exfoliated clay

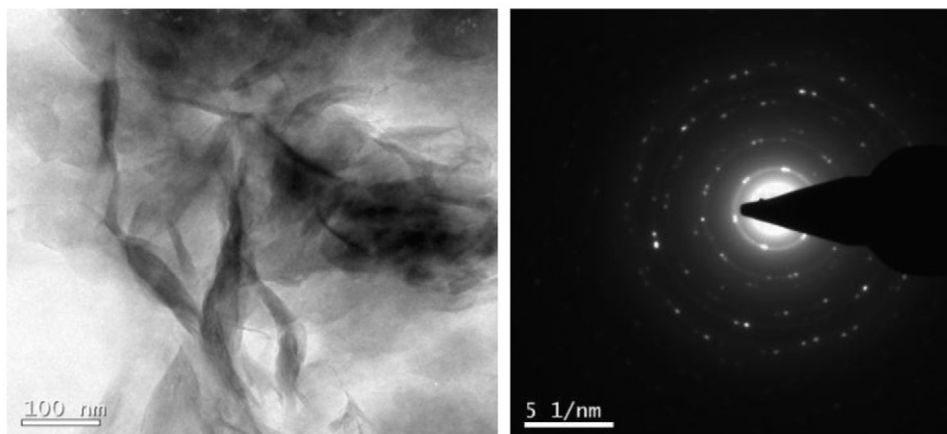
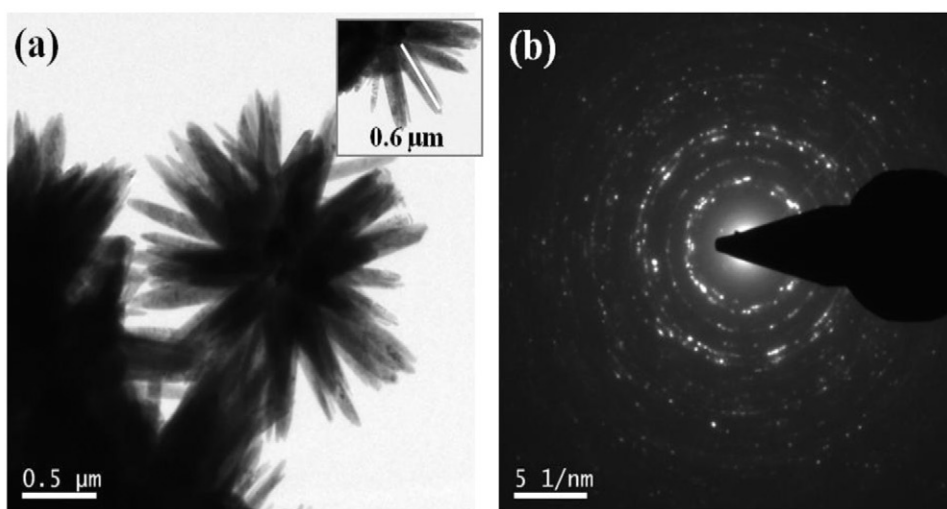
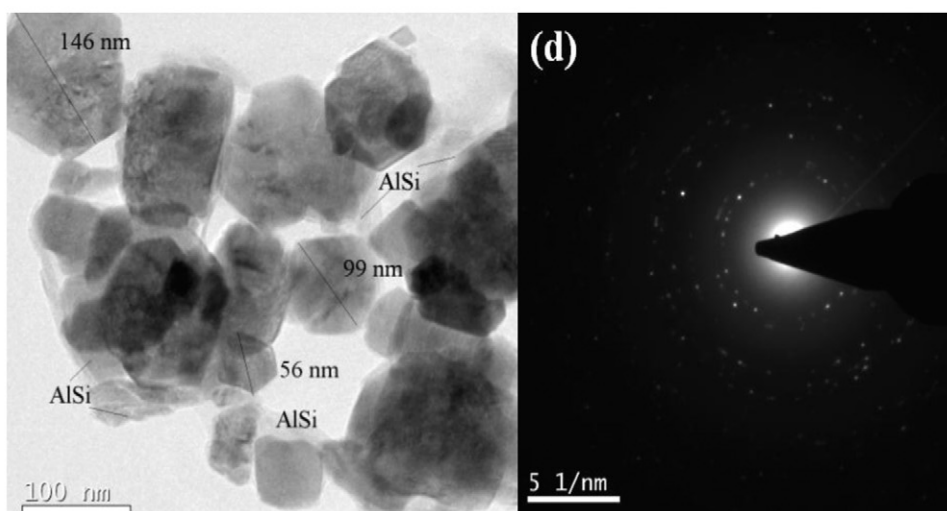
AlSi**ZnO****ZnO@AlSi**

Fig. 1. TEM and SAED pattern for AlSi, ZnO and ZnO@AlSi.

crystallites. Since TEM and PCS shown slightly larger ZnO particles in the range of 140 nm, and the XRD confirms the well defined crystalline peaks of both ZnO and AlSi, hybrid it could also expect that larger ZnO particles exist on the AlSi surface in a well dispersed manner as well. The prime advantage of this intercalation

assisted in situ growth technique is that the size and shape controlled ZnO crystallites and their uniform distribution throughout the surface and bulk even though they were not uniform in dimension and a schematic of hybrid structure of AlSi was proposed in Fig. 2(b).

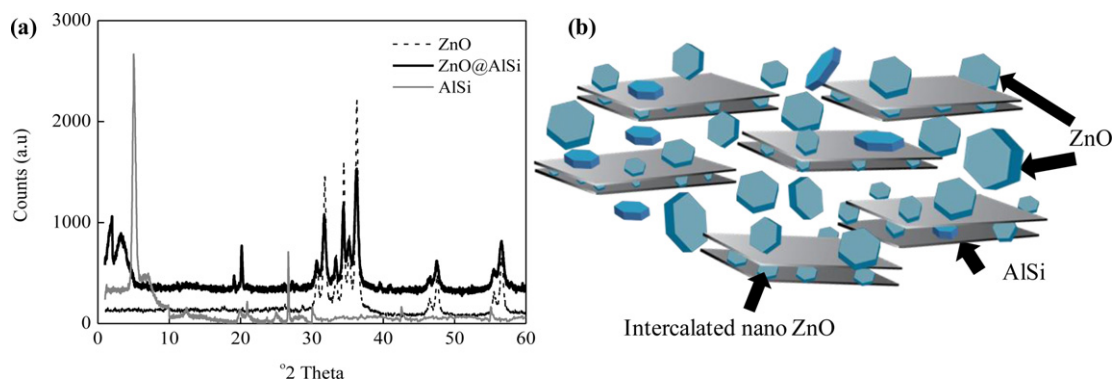


Fig. 2. XRD pattern for AlSi, ZnO and ZnO@AlSi (a) and proposed schematic of ZnO@AlSi (b).

The thermal decomposition of the AlSi, ZnO and ZnO@AlSi were shown in Fig S2. The thermogravimetric curve correspond to AlSi showed two-stage decompositions at 80–120 and 120–500 °C with a weight loss of 7.25 and 5.31%, respectively, which may be due to thermal evolution of moisture and interlayer water and structural OH groups, respectively [20]. About 2.24% weight loss could be seen in the TG of ZnO in the temperature range 80–150 °C, which might be attributed to the decomposition of physisorbed moisture. Another weight loss of ~3.05% was observed in the temperature range 150–400 °C, probably correspond to the decomposition of PEG capping, which was not removed during washing. The weight loss between 200–270 °C represented the decomposition of the condensation dehydration of the hydroxyls, as reported by Chen et al. [25]. The TGA of ZnO@AlSi showed almost same thermal response like that of ZnO, with two decomposition stages; 30–150 °C and 250–430 °C with weight loss of 2.3 and 3.59%, respectively. The enhanced thermal stability showed by ZnO@AlSi than precursor AlSi can be assumed to be the result of a hybrid intercalated structure resulted by the complete exchange of interlayer water molecules with nano ZnO.

3.2. N_2 -adsorption/desorption isotherm and optical properties

Fig. 3(a) represents the N_2 -adsorption/desorption isotherms for ZnO, AlSi and ZnO@AlSi hybrids. As shown, ZnO, AlSi and ZnO@AlSi showed type IV behaviour typical of mesoporous systems, but with hysteresis loops differ in shape. ZnO@AlSi showed H1 hysteresis loop (as recommended in the IUPAC manual), in which adsorption and desorption branches are almost parallel and nearly vertical over an appreciable range of gas uptake, indicating spheroidal clusters of fairly uniform size and array. ZnO and AlSi showed H2 hysteresis loop in which adsorption and desorption branches are

almost horizontal and nearly parallel over an appreciable range of gas uptake. H2 loops are generally found in corpuscular systems in which the distribution of pore size and shape is not so well defined [26]. The pore size distribution curve shown in Fig. 3(b) also evidenced that the pores of ZnO, AlSi and ZnO@AlSi were in typical mesoporous region of 2–4 nm. The isotherm further showed the ZnO@AlSi hybrid having large volume which is indicative of its high surface area. BET surface area followed the order: ZnO@AlSi > AlSi > ZnO. Specific surface area of AlSi and ZnO was 24.78 m²/g and 8.01 m²/g respectively. In hybrid structure it was increased to ZnO@AlSi as 40.35 m²/g. The increased surface area was advantages in the sense that higher availability of catalyst sites would aid an enhanced adsorption and photocatalytic decomposition.

The energy gap (E_g) of the hybrid ZnO@AlSi was evaluated using diffuse reflectance spectral (DRS) studies because silicate layer may have direct influence on the semiconducting activity (Fig. 4(a)). DRS was selected since it takes advantage of the enhanced scattering phenomenon in powder materials and hence effects of light scattering in the absorption spectra of powder samples dispersed in liquid media can be avoided [27]. Kubelka–Munk treatment was also carried out to extract E_g from DRS data at any wavelength as per the mathematical expressions given below [28]:

$$\frac{K}{S} = \frac{(1 - R_\infty)^2}{2R_\infty} \equiv F(R_\infty) \quad (1)$$

where K and S are absorption coefficient and K–M scattering, respectively, and $F(R_\infty)$ is Kubelka–Munk function:

$$R_\infty = \frac{R_{\text{sample}}}{R_{\text{standard}}} \quad (2)$$

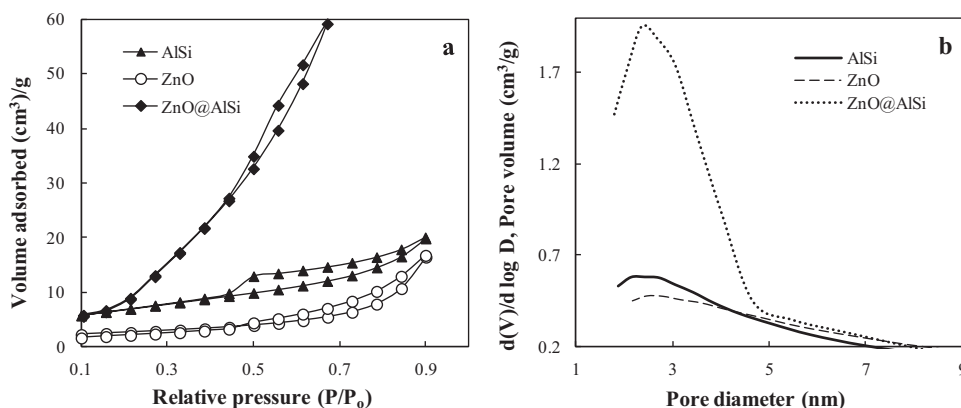


Fig. 3. BET surface area (a) and pore size distribution (b) plots for nitrogen adsorption/desorption onto AlSi, ZnO and ZnO@AlSi.

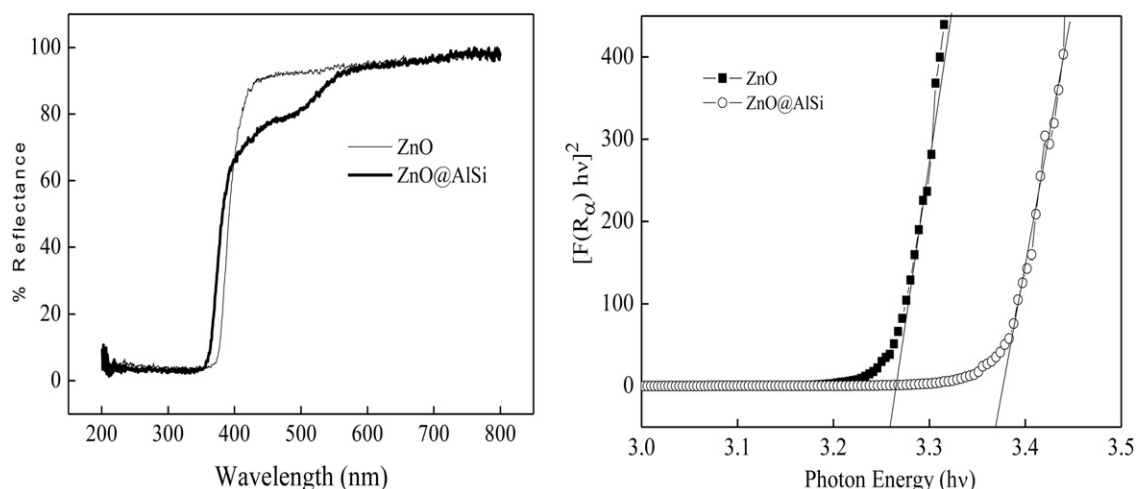


Fig. 4. DRS (a) and Kubelka–Munk transformed reflectance spectra (b) of ZnO and ZnO@AlSi.

For direct band gap semiconductors like ZnO, the Eq (1) can be developed as:

$$[F(R_\infty)hv]^2 = C(h\nu - E_g) \quad (3)$$

DRS of ZnO and ZnO@AlSi after Kubelka–Munk treatment was shown in Fig. 4(b). The intersection between the linear fit and the photon energy axis gave the E_g value as 3.27 and 3.36, to ZnO and ZnO@AlSi, respectively. Similar blue shift was observed by few other researchers when submicronic ZnO particles were immobilized in an inorganic matrix like silica [15,29]. The difference in the E_g value of ZnO compared to ZnO@AlSi might be induced by aggregated structures, and hence it can be assumed that electron tunnelling would have taken place due to the overlapping of the electron clouds of multi-stacked nanoclusters.

The photoluminescence properties of both ZnO and ZnO@AlSi hybrids were shown in Fig. S3. At the excitation wave length of 380 nm, multiple visible emission bands had been observed for both ZnO and ZnO@AlSi. More intense peaks at the photo energy values of 2.87 (432 nm), 2.55 (486 nm), 2.38 (520 nm) and a less intense shoulder peak at 2.32 eV (534 nm) were clearly seen in the PL spectrum. Generally, visible emissions in ZnO nanostructures are assigned for the surface oxygen vacancies [30]. Here we found that the ZnO trapped @AlSi interlayers had exhibited stronger fluorescence in the visible spectrum than the freely grown ZnO. In addition to the fine crystallite size of nano ZnO, the nano AlSi also significantly contribute to increase the defects concentration and oxygen vacancies that finally showed strong fluorescence [31]. Infact the AlSi favour in protecting the ZnO luminescence by controlling the exciton charge separation [32]. The PL emission reveals that the ZnO@AlSi may be exploited for promising uses as fluorescence labels and as phosphor materials. In this line, studies are initiated to further sensitize the nano ZnO@AlSi hybrids with some organic functional dyes.

In addition to the confirmation of luminescence properties the results obtained from the PL study also showed that the AlSi layers did not harm the semiconductivity of embedded ZnO, instead enhanced its photoactivity. Such tailored hybrid structure would perform multitasking like absorption, swelling, photo decomposition and photoreduction. AlSi are natural adsorbents but they do not show either catalytic reduction or decomposition. Similarly the ZnO is very poor in adsorption of metal ions and organics but show excellent catalytic activity. Both these functionalities can be reached in hybrid structures. Hence the nano ZnO@AlSi is a dual functional sorbent-catalyst which was validated by the

simultaneous adsorption, reduction and decomposition of metal ions and organics such as dyes and phenol.

3.3. Validation of dual functional nano ZnO@AlSi catalyst

3.3.1. Decontamination of water polluted with MB

Initial adsorption/photocatalytic validation experiments were conducted with aqueous solution of MB. MB removal capacity under dark condition, which can be accounted as adsorption capacity followed the order: ZnO@AlSi > AlSi > ZnO. It was seen (Fig. 5) that while AlSi and ZnO@AlSi could remove 25.84 and 68.92% of MB respectively, the single phase ZnO could remove only 9.51%. This was expected since BET surface area was greater for ZnO@AlSi than AlSi and ZnO.

As shown in Fig. 4(a), a small but broad background absorption in visible region was observed in the DRS of ZnO@AlSi, may be due to the presence of AlSi, indicating visible light activity and the blue shift of band gap at the same time indicated strong UV-light activity. Hence photocatalytic experiments were conducted under UV and visible light independently after keeping the catalysts and MB in contact for an equilibrium time of 2 h under dark in order to exclude the adsorption interference and the results are presented in Fig. 5. Almost 99.78% MB dye was degraded from test solution by using ZnO@AlSi, under UV-light irradiation, while

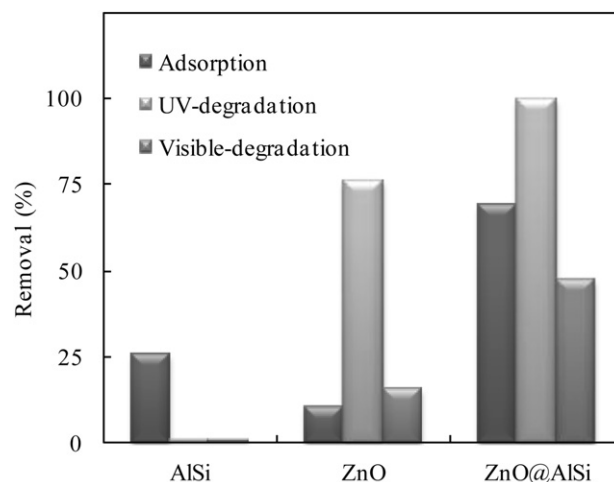


Fig. 5. Removal of MB from aqueous solution using AlSi, ZnO and ZnO@AlSi. Initial MB concentration: 50 mg/L; catalyst dose: 2 g/L, equilibrium time: 2 hr.

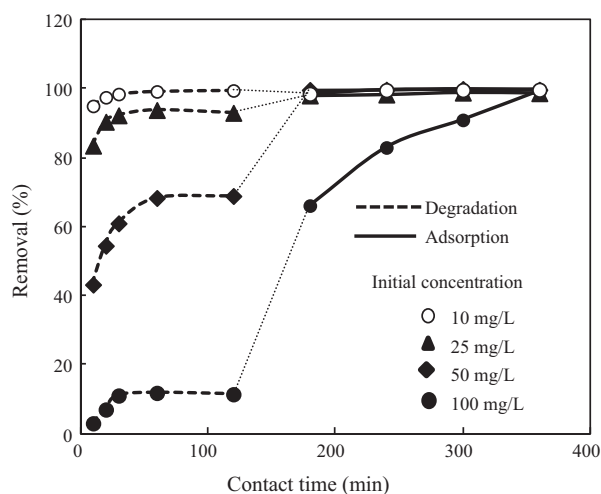


Fig. 6. Removal of MB by adsorption and photo-catalysis under UV-irradiation with time at different initial concentration. Catalyst dose: 2 g/L.

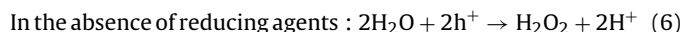
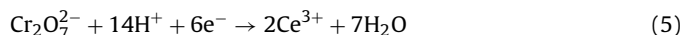
under visible light irradiation the degradation was 47.61%. On the other hand, ZnO showed MB degradation upto 76.78% under UV-light and 15.65% under visible light. The visible light activity of ZnO@AlSi can be attributed to an extension of the ZnO absorption in presence of AlSi into the visible region as a result of introducing localized levels which do not act as recombination centres. As expected, AlSi showed no removal effect under UV-light, indicating that the presence of semiconductor catalyst was indispensable for the photocatalytic degradation. These experiments indicated that the combination of ZnO and AlSi would be useful for the removal of pollutants in combined form than independently. In photocatalytic process, the reaction rate increases with pollutant concentration until it reaches a maximum and then stabilizes because the active sites of catalyst are saturated, so the high pollutant concentration kept on catalyst surface by adsorption can enhance the photocatalytic reaction rate and maintain the treatment efficiency. From the above results it can be confirmed that the simultaneous surface adsorption and photo degradation is responsible for the decontamination efficiency of ZnO@AlSi. Since the photodegradation driven by UV-light was twofold greater than visible light, all other photocatalytic experiments cited in this work, were done under UV-light only, unless otherwise stated.

The adsorption and photo catalytic capacities as a function of time for the ZnO@AlSi are shown in Fig. 6. These kinetic curves indicated that MB removal rate reached equilibrium in 2 h irrespective of initial MB concentration. Further adsorption was not detected with increase of contact time. Hence for all the studies here after 2 h adsorption was fixed prior to photo catalysis. Interestingly, at higher MB concentration, the photo catalysis was more effective than adsorption. It can be concluded that for the treatment of water that contaminated with high concentration of MB, synergic adsorption and photo decomposition may be ideal using ZnO@AlSi. This nanocatalyst was found very effective because almost complete removal of MB from aqueous solution of initial concentration 10 to 50 mg/L was obtained in 2 h adsorption and consecutive 2 h photo induced decomposition. At high concentrations, say for 100 mg/L of MB solution, complete decontamination was seen with 4 h photo catalysis, indicating that photocatalytic efficiency of ZnO@AlSi depend on irradiation time.

3.3.2. Detoxification of water polluted with Cr(VI)

From the literature, studies considering optimum range of pH for the photocatalytic reduction of Cr(VI) using ZnO was rather limited. Hence we initially carried out adsorption and photo catalysis

separately with 2 g/L ZnO@AlSi exposed to 25 mg/L of Cr(VI) solution at different pH (Fig. S4(a) and (b)). In the case of adsorption, Cr(VI) was removed from the solution but adsorbed onto the pores of the catalyst and in the case of photo catalysis, Cr(VI) was removed from the catalyst surface via reduction to Cr(III). As shown, Cr(VI) was best removed (~99.9%) from solution both by adsorption and photo catalysis, at pH 3.0. Cr(T) which is the sum of Cr(VI) and Cr(III) was obtained from AAS analysis confirmed the presence of Cr(III) in the supernatant solution after photocatalysis. ZnO generally dissolves at a low pH and a high pH is detrimental to both the catalyst and the oxidizing species. Some authors reported low photo reduction of Cr(VI) and 'photo corrosion' of ZnO at neutral to basic pH [33]. In our studies, we observed that increasing pH above 4.0 caused a drastic reduction in the removal efficiency of ZnO@AlSi, which we would like to attribute to the pH_{ZPC} equals to 4.2 of ZnO@AlSi. Below pH 4.2, the catalyst surface was positive and above 4.2, it was negative. We did not observe any dissolution of catalyst at pH 3.0, may be due to hybridization of ZnO with AlSi and hence hereafter performed all our experiments with Cr(VI) at a constant pH 3.0. Any other researchers did not reported Cr(VI) reduction at this low pH with ZnO to the best of our knowledge, even though some has been reported at a pH as low as 2.0 with TiO₂ [34,35]. In the presence of photocatalyst, Cr(VI) can be reduced to Cr(III) by the excited electrons, upon UV irradiation but the mechanism, though not very clear, could be described as the capture of photo-excited conduction band electrons followed by reduction. At pH 3.0, the possible species of chromium are $HCrO_4^-$, $Cr_2O_7^{2-}$, $Cr_3O_{10}^{2-}$ and $Cr_4O_{13}^{2-}$, among which the one which predominating between pH 2.0 and 6.0 was $Cr_2O_7^{2-}$ [17,36]. Hence the possible mechanism proposed was as follows:



As shown in Fig. 7 adsorption of Cr(VI), executed under dark condition reached equilibrium at about 60 to 90 min, quite independent of initial concentration. Removal of Cr(VI) decreased from 55.72 to 24.89% when initial concentration increased from 10 to 100 mg/L, may be due to the increased competition for the fixed number of the active sites on the adsorbent surface. A drastic reduction in the concentration of Cr(VI) was observed upon 1 h UV illumination. Difference in the removal% of Cr(VI) could be accountable as reduction to Cr(III), since adsorption indicated saturation in 60 min of contact under dark. No trace of Cr(VI) was obtained after UV illumination of 2 h for Cr(VI) of initial concentration 10 and 25 mg/L, while 3 h and 5 h of UV-illumination is needed for 50 and 100 mg/L, respectively. The results confirmed that reduction of Cr(VI) to Cr(III) is directly related to the illumination time.

3.4. Analysis of kinetic rate of reduction

The experimental data from photocatalytic process was further used to analyze the rate of photocatalytic reduction of Cr(VI), by using the Langmuir–Hinshelwood kinetic rate equation, which is well acknowledged for photocatalytic reaction [17] and is given as:

$$\frac{dC}{dt} = k_{app}C \quad (7)$$

where ' dC/dt ' represents the rate of change in the Cr(VI) concentration with respect to ' t ' the UV illumination time. k_{app} the apparent first-order reaction rate constant, and ' C ' the concentration of Cr(VI). On integrating the above equation and

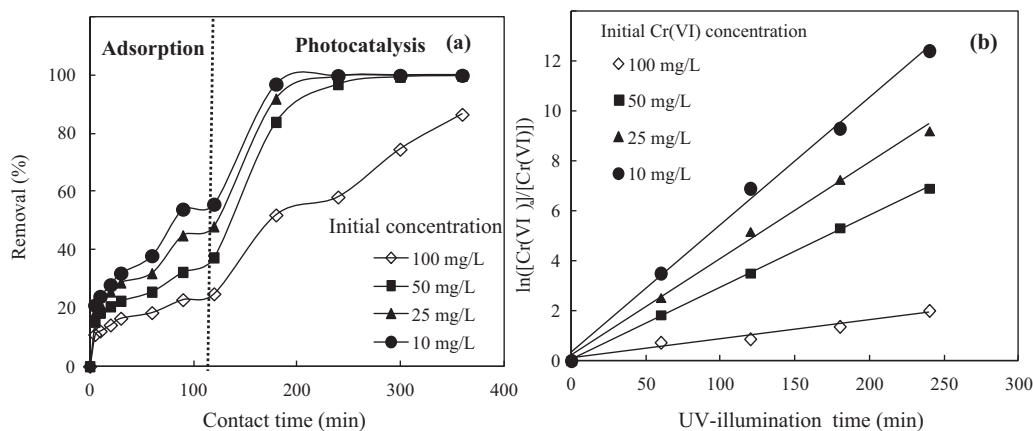


Fig. 7. Removal of Cr(VI) from aqueous solution (upto 120 min under dark, 120–340 min under UV-illumination) with respect to contact time (a) Typical Langmuir–Hinshelwood plot for determination of kinetic rate of Cr(VI) reduction in aqueous solution (b) by ZnO@AlSi at varying initial concentrations; pH 3.0, catalyst dose: 2 g/L.

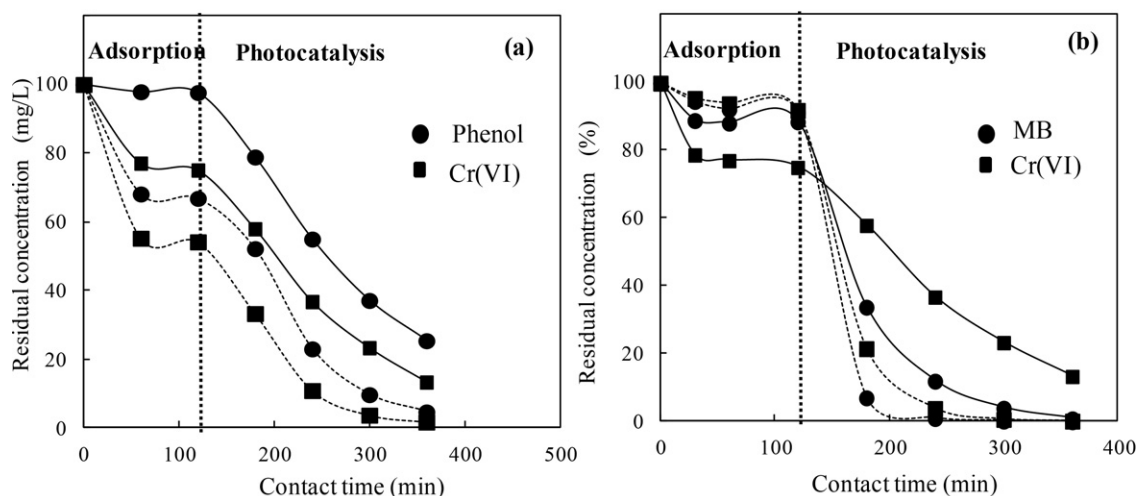


Fig. 8. Variation in the residual Cr(VI) and phenol concentration in Cr(VI)/phenol bicomponent system (a) variation in the residual Cr(VI) and MB concentration in Cr(VI)/MB system (b) with respect to contact time (upto 120 min under dark, 120–340 min under UV-illumination) by ZnO@AlSi. Dotted line represent a bi-component photocatalytic system and solid line present single component system containing either Cr(VI), phenol or MB.

rephrasing in the present context, the following equation is obtained:

$$\ln \frac{[\text{Cr(VI)}]_0}{[\text{Cr(VI)}]} = k_{\text{red}} t_{\text{UV}} \quad (8)$$

The plot of $\ln ([\text{Cr(VI)}]_0/[\text{Cr(VI)}])$ with UV illumination time gave straight lines, as shown in Fig. 7(b), confirming the first order reduction of Cr(VI) to Cr(III). The rate constants are presented in Table 1. As shown apparent rate constant of the Cr(VI) reduction got decreased at high Cr(VI) concentration. Similar results were reported by many other researchers. The reason for this phenomenon was accounted as interception of UV-radiation, since the absorbance of the solution increased with Cr(VI) concentration

and thereby diminishing the conversion and catalysis efficiency [36–39].

3.5. Synergistic photocatalytic effect between Cr(VI) and phenol

In order to accelerate the photocatalytic reduction of metal ions, many organic acids and alcohols were reported to be added in aqueous solution to serve as hole scavengers to inhibit the recombination of electrons and holes but the kinetic information on the effect of these organic compounds on the photocatalytic reduction of metal ion is scarce. In the present study, phenol, was chosen as the additional electron donor in the Cr(VI)/ZnO@AlSi photocatalytic system and was expected to serve as the hole scavenger to inhibit the recombination of electrons and holes. Thus possibility of the capture of electron by Cr(VI) could be promoted while the parts of hole was scavenged by phenol, and the photo reduction reaction rate of Cr(VI) was subsequently increased. Fig. 8(a) showed the reduction profiles of Cr(VI), with an initial concentration of 25 mg/L, in the absence and presence of phenol of same concentration. Comparing the initial rates of Cr(VI) reduction (Table 2), it was obvious that the presence of phenol increased the degradation rate of Cr(VI), and at the same time phenol, which itself was a potential pollutant under the voc category, got degraded and declined in concentration.

Table 1

The pseudo-first-order reduction rate constants of Cr(VI) by ZnO@AlSi at various initial concentration at pH: 3.0.

Concentration (mg/L)	k_{red} (min^{-1})	R^2
10	5.11×10^{-2}	0.981
25	3.85×10^{-2}	0.999
50	2.88×10^{-2}	0.995
100	7.76×10^{-3}	0.996

Table 2
The pseudo-first-order rate constants for reduction of Cr(VI) and oxidation of phenol by ZnO@AlSi in single and binary component systems.

System	Component	Concentration (mg/L)	$k_{\text{red/oxn}}$ (min ⁻¹)	R^2
Binary (Cr(VI) + Phenol)	Cr(VI)	100	1.72×10^{-2}	0.998
	Phenol	100	1.29×10^{-2}	0.996
Single component	Cr(VI)	100	8.21×10^{-3}	0.998
	Phenol	100	5.82×10^{-3}	0.992

Table 3
The pseudo-first-order rate constants for reduction of Cr(VI) and oxidation of MB by ZnO@AlSi in single and binary component systems.

System	Component	Concentration (mg/L)	Dose (g/L)	$k_{\text{red/oxn}}$ (min ⁻¹)	R^2
Binary (Phenol + MB)	Cr(VI)	100	2	2.61×10^{-2}	0.997
	MB	100	2	3.28×10^{-2}	0.991
Single component	Cr(VI)	100	2	8.21×10^{-3}	0.994
	MB	100	2	1.92×10^{-2}	0.998

3.6. Synergistic photocatalytic effect between Cr(VI) and MB

The synergic effect was also attempted on the photo efficiency of ZnO@AlSi for Cr(VI) reduction with the presence of dye (MB). As expected, photocatalytic reduction of Cr(VI) was found to be more efficient in the Cr(VI)/MB system than in the single system because of the promoter effect by photocatalytic degradation of the dye (Fig. 8 b). Comparison of Cr(VI)/phenol and Cr(VI)/MB system indicated that the photo reduction of Cr(VI) in the binary system was significantly faster than the single system. The photocatalytic reduction rate of Cr(VI) increased from 8.21×10^{-3} to 2.61×10^{-2} and 1.72×10^{-2} with MB and phenol, respectively. In metal ion-organic compound system, organics receives holes from the valance band directly or indirectly and get oxidized. In the present study, we could assume that the oxidation of MB consumed photo-excited holes more efficiently than phenol and impeded electron–hole recombination which eventually resulted in enhanced photocatalytic Cr(VI) reduction [36]. Reason behind this assumption is that MB showed higher affinity to ZnO@AlSi surface than phenol as evidenced from the initial adsorption in the dark. Interestingly, presence of Cr(VI) also resulted in increased photo-oxidation of MB and phenol (Table 3), which could be ascribed to fast reaction in the photo-generated hole in presence of Cr(VI).

3.7. Reusability of ZnO@AlSi

In order to check whether the ZnO@AlSi could be used for multiple cycles of operation, repeated three cycles of adsorption/photocatalysis experiments were carried out with same catalyst. Results obtained for the three single component pollutant systems (Cr(VI), MB and phenol) and two bi-components pollutant systems (Cr(VI)/phenol and Cr(VI)/MB) from three cycles of experiments were given in Fig. 9. As shown, ZnO@AlSi could retain its

activity fairly well in single component pollutant systems even after three cycles of application, but in bi-component systems, the catalytic activity of ZnO@AlSi was found to decrease after each cycles. The reduction in activity may be accounted as degradation of catalyst, since in metal–organic pollutant system, the electron–hole pair recombination was retarded effectively and hence eventually the catalyst life time got decreased. But still >75% of degradation of Cr(VI), MB and phenol (initial concentration 100 mg/L) was observed in bi-component pollutant systems indicating ZnO@AlSi as a potential recyclable catalyst for complex pollutant systems. The result from this study will be constructive for integration of photocatalytic systems onto real wastewater treatment applications, principally for industries.

4. Conclusions

In an attempt to engineer a photocatalyst that is more effective for the removal of inorganic (Cr(VI)) and organic (MB and phenol) pollutants from contaminated wastewater, we developed mesoporous, hybrid ZnO@AlSi, consisted of nanoparticulate zinc oxide (ZnO) embedded in aluminosilicate matrix (AlSi). The PEG capped zinc precursor was intercalated with in AlSi and transformed to well crystalline nano ZnO via microwave irradiation. The in situ growth of ZnO increased the interlayer basal spacing showed restricted growth of ZnO nanoparticle and increased bulk surface area. ZnO@AlSi is well characterized to analyze its structural, morphological, thermal, optical and chemical properties. It was confirmatively seen that ZnO@AlSi could perform photo oxidation of MB and photoreduction of Cr(VI) together in presence of UV irradiation. The reaction rate increased with pollutant concentration until it reaches a maximum and then stabilizes upon saturation of active sites of catalyst. Cr(VI) is best removed (~99.9%) from solution both by adsorption and photo catalysis, at pH 3.0 and rate of reduction was found to increase with illumination time. Langmuir–Hinshelwood kinetic rate equation was found to describe the photoactivity of ZnO@AlSi. The synergic photooxidation and reduction activity of ZnO@AlSi was confirmed in bi-component Cr(VI)/phenol and Cr(VI)/MB systems. In the presence of phenol and MB the degradation rate of Cr(VI) was increased and at the same time phenol and MB which itself were a potential pollutants got degraded and declined in concentration. Photo reduction of Cr(VI) in the binary system is significantly faster than the single system, since photooxidation of MB and phenol consumed excited holes and hence impeded electron–hole recombination which eventually resulted in enhanced photocatalytic Cr(VI) reduction. Reusability studies indicated that lifetime of the catalyst got decreased in inorganic-organic pollutant systems, compared to single component systems. The study systematically showed the design and synthesis of economically viable eco catalyst

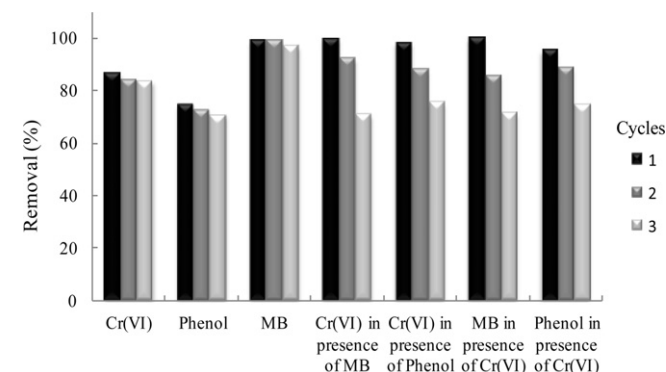


Fig. 9. Recyclability of ZnO@AlSi in both single and bi-component pollutant systems.

for detoxification of hazardous pollutants via one step adsorption, photo reduction and decomposition together.

Acknowledgements

The authors thank Director, NIIST-Trivandrum for providing laboratory facilities. P. S. Suchithra is grateful to Council of Scientific and Industrial Research (CSIR), Government of India, New Delhi for providing CSIR–Nehru Science Postdoctoral Research Fellowship to carry out this work and to Dr. K.G.K. Warriar, Dr. S. Ghosh and Dr. S. Shukla for valuable suggestions and encouragement. We acknowledge technical supports from Mr. Kiran Mohan and Mr. Guruswamy for TEM and XRD, respectively.

Appendix A. Supplementary data

Supplementary data associated with this article can be found, in the online version, at <http://dx.doi.org/10.1016/j.apcatb.2012.10.010>.

References

- [1] A.L. Rowbotham, L.S. Levy, L.K. Shuker, *Journal of Toxicology and Environmental Health*, Part B 3 (2000) 145–178.
- [2] P. Mytych, Z. Stasicka, *Applied Catalysis B* 52 (2004) 167–172.
- [3] USEPA, *Ambient Water Quality Criteria For Chromium, PC31*, EPA440/5-80-035, 1980.
- [4] WHO, *Guidelines for Drinking Water Quality*, World Health Organisation, Geneva, 1993.
- [5] M. Albert, M.S. Lessin, B.F. Gilchrist, *Journal of Pediatric Surgery* 38 (2003) 1244–1245.
- [6] E. Lopez, B. Soto, M. Arias, A. Noez, D. Rubinos, M.T. Barral, *Water Research* 32 (1998) 1314–1322.
- [7] A. Ozcan, E.M. Oncu, A.S. Ozcan, *Journal of Hazardous Materials* 129 (2006) 244–252.
- [8] J. Bujdak, N. Iyi, *Clays and Clay Minerals* 50 (2002) 446–454.
- [9] A. Fujishima, T.N. Rao, D.A. Tryk, *Journal of Photochemistry and Photobiology C* 1 (2000) 1–21.
- [10] M. Nirmala, M.G. Nair, K. Rekha, A. Anukaliani, S.K. Samdarshi, R.G. Nair, *African Journal of Basic & Applied Sciences* 2 (2010) 161–166.
- [11] G.D. Mihai, V. Meynen, M. Mertens, N. Bilba, P. Cool, E.F. Vansant, *Journal of Materials Science* 45 (2010) 5786–5794.
- [12] C.H. Wu, C.F. Wu, J.F. Shr, C.T. Hsieh, *Separation and Purification Technology* 61 (2008) 258–265.
- [13] J. Nemeth, G. Rodriguez-Gattorno, D. Daaz, A.R. Vazquez-Olmos, I. Dekany, *Langmuir* 20 (2004) 2855–2860.
- [14] S.G. Hur, T.W. Kim, S.J. Hwang, S.H. Hwang, J.H. Yang, J.H. Choy, *Journal of Physical Chemistry B* 110 (2006) 1599–1604.
- [15] I. Fatimah, W. Shaobin, D. Wulandari, *Applied Clay Science* 53 (2011) 553–560.
- [16] S. Meshram, R. Limaye, S. Ghodke, S. Nigam, S. Sonawane, R. Chikate, *Chemical Engineering Journal* 172 (2011) 1008–1015.
- [17] Y. Ku, I.-L. Jung, *Water Research* 35 (2001) 135–142.
- [18] X.-R. Xu, H.-B. Li, J.-D. Gu, *Chemosphere* 63 (2006) 254–260.
- [19] J.M. Meichtry, M. Brusa, G. Mailhot, M.A. Grela, M.I. Litter, *Applied Catalysis B* 71 (2007) 101–107.
- [20] T.S. Anirudhan, P.S. Suchithra, *Journal of Industrial and Engineering Chemistry* 16 (2010) 130–139.
- [21] L. Zampori, P.G. Stampino, C. Cristiani, P. Cazzola, G. Dotelli, *Applied Clay Science* 50 (2010) 266–270.
- [22] A. Alemdar, N. Gungor, O.I. Ece, O. Atici, *Journal of Materials Science* 40 (2005) 171–177.
- [23] H. Zhang, D. Yang, X. Ma, Y. Ji, J. Xu, D. Que, *Nanotechnology* 15 (2004) 622.
- [24] H. Zhang, D. Yang, S. Li, X. Ma, Y. Ji, J. Xu, D. Que, *Materials Letters* 59 (2005) 1696–1700.
- [25] J. Cheng, R. Guo, Q.M. Wang, *Applied Physics Letters* 85 (2004) 5140–5142.
- [26] S.J. Gregg, K.S.W. Sing, *Adsorption, Surface Area, and Porosity*, 2nd ed., Academic Press, 1983.
- [27] A.E. Morales, E.S. Mora, U. Pal, *Revista Mexicana de Fisica* 53 (2007) 18.
- [28] P. Kubelka, F. Munk, *Zeitschrift fur technische Physik* 12 (1931) 593–601.
- [29] J. Zhai, X. Tao, Y. Pu, X.F. Zeng, J.F. Chen, *Applied Surface Science* 257 (2010) 393–397.
- [30] W.Q. Peng, S.C. Qu, G.W. Cong, Z.G. Wang, *Materials Science in Semiconductor Processing* 9 (2006) 156–159.
- [31] M. Abdullah, T. Morimoto, K. Okuyama, *Advanced Functional Materials* 13 (2003) 800–804.
- [32] H.M. Xiong, *Journal of Materials Chemistry* 20 (2010) 4251–4262.
- [33] X. Wang, S.O. Pehkonen, K. Ajay, *Industrial and Engineering Chemistry Research* 43 (2004) 1665–1672.
- [34] F. Jiang, Z. Zheng, Z. Xu, S. Zheng, Z. Guo, L. Chen, *Journal of Hazardous Materials* 134 (2006) 94–103.
- [35] J.A. Navio, J.J. Testa, P. Djedjeian, J.R. Padron, D. Rodriguez, M.I. Litter, *Applied Catalysis A* 178 (1999) 191–203.
- [36] S.G. Schrank, H.J. Jos, R. Moreira, *Journal of Photochemistry and Photobiology A: Chemistry* 147 (2002) 71–76.
- [37] T. Iwata, M. Ishikawa, R. Ichino, M. Okido, *Surface and Coatings Technology* 169 (2003) 703–706.
- [38] S. Chakrabarti, B.K. Dutta, *Journal of Hazardous Materials* 112 (2004) 269–278.
- [39] N. Wang, L. Zhu, K. Deng, Y. She, Y. Yu, H. Tang, *Applied Catalysis B* 95 (2010) 400–407.